ELSEVIER

Contents lists available at ScienceDirect

Journal of Sound and Vibration

journal homepage: www.elsevier.com/locate/jsvi



Acoustic-electroelastic interactions in ultrasound energy transfer systems: Reduced-order modeling and experiment



Vamsi C. Meesala ^a, Saad Ragab ^a, Muhammad R. Haji ^b, Shima Shahab ^{a,c,*}

- ^a Department of Biomedical Engineering and Mechanics, Virginia Tech, Blacksburg, VA, 24060, USA
- b Department of Civil, Environmental and Ocean Engineering, Davidson Laboratory, Stevens Institute of Technology, NJ, 07030, USA
- ^c Department of Mechanical Engineering, Virginia Tech, Blacksburg, VA, 24060, USA

ARTICLE INFO

Article history: Received 8 November 2019 Revised 11 February 2020 Accepted 12 February 2020 Available online 25 February 2020 Handling Editor: Erasmo Carrera

Keywords:
Contactless energy transfer
Ultrasound acoustic energy transfer (UAET)
Reduced-order models
Acoustic-structure interactions
Electrical impedance

Piezoelectric finite element modeling

ABSTRACT

Contactless ultrasound energy transfer from a piezoelectric cylinder or disk subjected to forced vibrations to a piezoelectric receiver offers the capability of safely transferring energy to sensors and devices, which is of great interest in different applications. Physical processes supporting ultrasonic energy transfer include piezoelectric-generated vibrations at a transmitting element, piezoelectric transduction of elastic vibrations at a receiving element, acoustic wave propagation, and acoustic-structure interactions at the surfaces of the transmitting and receiving elements. Considering these processes, we present an experimentally-validated multi-physics model that fills a knowledge gap in terms of accurately representing the fluidloaded response of piezoelectric disks, usually used in ultrasonic energy transfer as a cylindrical transmitting source-cylindrical receiver combination. First, we derive the governing equations using the generalized Hamilton's principle and solve them using the finite element method. Second, we compute the surface pressure distribution due to acoustic-structure interactions under resonance conditions. We then use the mode shapes and surface pressure distributions obtained from the finite element model in conjunction with the matrix governing equations to develop a reduced-order model with quantified reactive and resistive parts of the acoustic radiation impedance. The developed reduced-order model is then experimentally validated by comparing the electrical impedance of four different piezoelectric disks having various aspect ratios. We also discuss how the proposed approach should be utilized to develop reduced-order model for piezoelectric receivers. The presented approach and reduced-order model allow for accurate identification of critical parameters that govern acoustic energy transfer between piezoelectric disks, which is crucial for designing efficient ultrasonic acoustic energy transfer systems.

© 2020 Elsevier Ltd. All rights reserved.

1. Introduction

Ultrasound acoustic energy transfer (UAET) is an emerging contactless energy transfer (CET) technology that offers the capability to safely power sensors and devices while eliminating the need to replace batteries, which is of interest in many applications. This technology provides efficient power transfer with deeper penetration depths and lower operating frequencies in comparison to the widely used electromagnetic CET technologies [1], particularly inductive coupling [2–9]. Recent investigations have suggested that UAET could be effectively used in biomedical applications to recharge low-power implanted medical

^{*} Corresponding author. Department of Mechanical Engineering, Virginia Tech, Blacksburg, VA, 24060, USA. E-mail address: sshahab@vt.edu (S. Shahab).

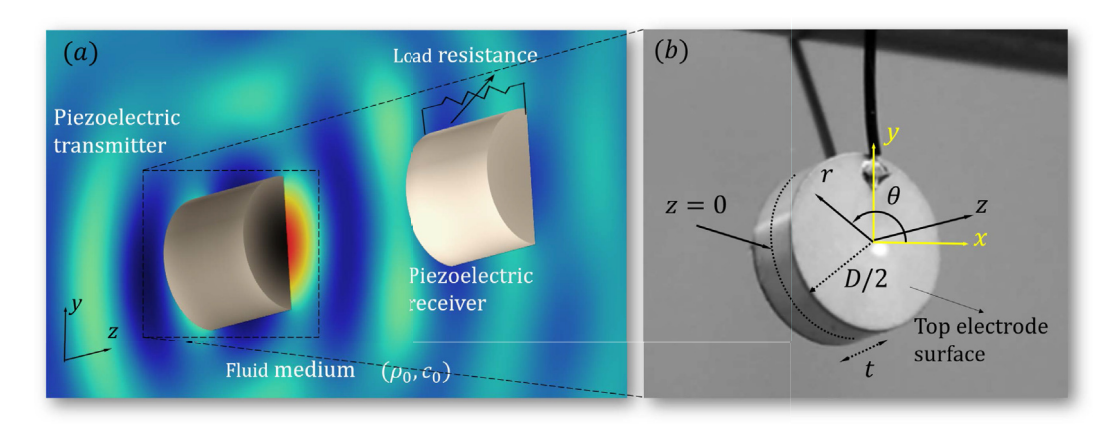


Fig. 1. (a) Snapshot of UAET with cylindrical transmitter and receiver and (b) piezoelectric disk with free-free boundary conditions showing the coordinate axes, (x, y, z) (r, θ, z) , considered for the analysis.

devices (e.g., 1μ W-10mW [10–12]), potentially eliminating the need for surgical procedures for battery replacement. These implanted medical devices can be designed for health monitoring, assisting in treatment, or improving the function of particular organs in the host's body [12–18]. For instance, transcutaneous UAET can be used to wirelessly power and communicate with neural interface systems providing a useful toolset to build long-lasting and reliable neural recording systems [14].

UAET is a multiphysics process that involves the domains of structural dynamics, piezoelectricity, and acoustic-structure interaction. In UAET systems, acoustic waves generated by a transmitter cause a piezoelectric receiver to vibrate and generate electrical power, thereby transferring energy from the transmitter to the receiver. As such, a typical UAET system consists of a transmitter, an acoustic medium that supports acoustic wave transmission, and a receiver with its electrical circuit (see Fig. 1 of Roes et al. [1]). Despite recent advances in UAET, the modeling efforts are lagging, and the current state-of-the-art experiments are mostly designed using primal understanding of underlying physics with a demonstrated low power-transfer efficiency [1,19]. In particular, the modeling challenges have limited the capability to obtain accurate solutions for the fluid-loaded vibrations of the receiver or transmitter and induced surface pressure distributions. The challenges can be better illustrated by considering a finite transversely isotropic piezoelectric disk, which is often used in proof-of-concept experiments [20-25]. Particularly, the equations governing the vibrations of the piezoelectric disk do not possess a closed-form solution without imposing assumptions or limitations on the dimensions of the disk [26-30]. One of these assumptions is the "piston-like" deformation assumption of the thickness mode, which converts the two-dimensional problem to a one-dimensional one and significantly simplifies the model. However, this assumption is satisfied only when the diameter to thickness ratio is more than twenty, D/t > 20 [31–33]. Moreover, the surface pressure distribution of an unbaffled non-planar structure, such as a thick disk, for a given deformation doesn't have an analytic closed-form expression, and one has to rely on the boundary element or finite element methods [34-40]. Finally, the reflected, scattered and blocked pressure distributions of the acoustic pressure field, that arise from the acoustic boundary conditions at the interfaces [41], should be accurately represented in any model to be used in optimizing the system's performance.

Acoustic-structure interaction models employed in the UAET can be classified into two main representations making different approximations. The first representation makes use of the symmetric nature of the "piston-like" deformation to approximate the acoustic structure interaction of an incoming plane wave as the sum of pressures due to the incident wave and radiated pressure from a baffled piston [20,21,24,25]. Such an approximation neglects the blocked pressure due to reflection and scattering. In the second representation, the boundary conditions are formulated by approximating the radiation pressure due to the vibration of the top and bottom surfaces of the disk to that of an infinite plate [22,23]. The experiments and experimentally-validated multiphysics reduced-order model (ROM), presented in this paper, aim at filling a knowledge gap in terms of accurately modeling resonant vibration modes associated with different UAET phenomena. Furthermore, the developed model captures the acoustic loading effects on piezoelectric disks submerged in a fluid by quantifying the resistive and reactive components of acoustic radiation impedance of the surrounding medium. The presented model enables the identification of critical parameters such as the radiation mass and radiation resistance which impact the energy transfer capabilities. As such, we investigate the effects of acoustic loading on a finite transversely isotropic piezoelectric disk that is submerged in a fluid. In particular, we develop an axisymmetric finite element method (FEM) model by using the generalized Hamilton's principle followed by condensation technique [31,42,43] to incorporate the radiation pressure of the disk in the surrounding fluid. Using the FEM model, we obtain a reduced-order model that accurately predicts the response near the resonant frequency of any relevant mode under electrical actuation. We hypothesize that the surface pressure distribution at the resonant frequency is sufficient to investigate the resonant response of the disk in a fluid medium. We then show that the surface pressure distribution in the FEM model corresponds to two parameters in the reduced-order model, R_{mode} , and X_{mode} , that respectively represent the resistive and reactive parts of acoustic radiation impedance. The efficacy of the proposed reduced-order model is experimentally demonstrated for the length expander mode of four disks differing in their dimensions under electrical actuation. This mode is the first axisymmetric vibrational mode exhibited by a piezoelectric disk [33]. We also discuss how the presented modeling approach to develop a reduced-order model can be utilized in the case of receivers. The approach involving the development of finite element-augmented reduced-order model is presented in Section 2 where we give details of the derivation of the governing equations for the vibrations of a piezoelectric disk. The developed FEM model to solve the governing equation is presented in Section 2.1. In Section 2.2, the challenge in determining the acoustic loading is highlighted, which is followed by details on the solution approach undertaken in this effort. The reduced-order model is then derived from the FEM model using the mode projection technique, which concludes the mathematical modeling framework. The versatility and accuracy of the FEM model in predicting the response characteristics of the disk including surface deformation, and electrical impedance are assessed through comparison with results from in-air experimental measurements as presented in Section 3.1. The reduced-order model of the acoustic structure interaction, which includes the acoustic loading effects, is validated with experimental results obtained from electrical impedance measurements for four different disks in deionized (DI) water in Section 3.2. A discussion of the advantages and shortcomings of the reduced-order model is also given in Section 3.2. The conclusions are summarized in Section 4.

2. Governing equations and reduced-order model

A schematic of a UAET system setup with cylindrical transmitter and receiver is shown in Fig. 1a. A transversely isotropic cylindrical disk of diameter *D*, and thickness *t*, with electrodes on top and bottom surfaces suspended freely in a fluid, as shown in Fig. 1b, is considered for the analysis and development of a reduced-order model. A general linear constitutive relation of piezoelectric material is used to investigate the response of the disk and is written in matrix form as

$$\sigma = \mathbf{C}^{\mathsf{E}}\mathbf{S} - \mathbf{e}\mathbf{E} \tag{1a}$$

$$\mathbf{D} = \mathbf{e}^{\mathsf{t}} \mathbf{S} + \varepsilon^{\mathsf{S}} \mathbf{E} \tag{1b}$$

where σ and \mathbf{S} are respectively the mechanical stress, and strain vectors; and \mathbf{D} and \mathbf{E} are respectively the associated electrical displacement and field vectors. The parameters \mathbf{C}^E , \mathbf{e} , and $\boldsymbol{\varepsilon}^S$ are respectively the stiffness at constant electric field, coupling parameter, and permittivity at constant strain matrices; and the superscript t is used to denote the transpose of the associated matrix.

A Cartesian coordinate system (x,y,z), with the z-axis along the thickness direction as shown in Fig. 1b is defined with the assumption that the material is isotropic in the xy plane, thereby allowing the assumption of axisymmetric response. As such, we solve only for variables in the radial r, and thickness z, directions in a cylindrical coordinate system, as shown in Fig. 1b. Further, considering a meridional plane (θ = constant) of the disk, the linear strain \mathbf{S} and stress $\boldsymbol{\sigma}$ are written in matrix notation as

$$\mathbf{S} \equiv \begin{cases} S_r \\ S_{\theta} \\ S_z \\ 2S_{z\theta} \\ 2S_{rz} \\ 2S_{r\theta} \end{cases} = \begin{bmatrix} \frac{\partial}{\partial r} & 0 \\ \frac{1}{r} & 0 \\ 0 & \frac{\partial}{\partial z} \\ 0 & 0 \\ \frac{\partial}{\partial z} & \frac{\partial}{\partial r} \\ 0 & 0 \end{bmatrix} \begin{cases} u \\ w \end{cases}, \quad \boldsymbol{\sigma} \equiv \begin{cases} \boldsymbol{\sigma_r} \\ \boldsymbol{\sigma_{\theta}} \\ \boldsymbol{\sigma_z} \\ \boldsymbol{\sigma_{z\theta}} \\ \boldsymbol{\sigma_{rz}} \\ \boldsymbol{\sigma_{r\theta}} \end{cases}$$
(2a)

where $u(\equiv u(r,z))$ and $w(\equiv w(r,z))$ are respectively the displacement components in the r, and z directions. The associated electric field is written as

$$\mathbf{E} = -\begin{cases} \frac{\partial}{\partial r} \\ \frac{\partial}{\partial z} \end{cases} \varphi \tag{2b}$$

where $\varphi(\equiv \varphi(r,z))$ is the electric potential, and \mathbf{C}^E , \mathbf{e} , and $\boldsymbol{\varepsilon}^S$ in Voigt notation are written as

$$\mathbf{C}^{E} = \begin{bmatrix} C_{11} & C_{12} & C_{13} & 0 & 0 & 0 \\ C_{12} & C_{11} & C_{13} & 0 & 0 & 0 \\ C_{13} & C_{13} & C_{33} & 0 & 0 & 0 \\ 0 & 0 & 0 & C_{44} & 0 & 0 \\ 0 & 0 & 0 & 0 & C_{44} & 0 \\ 0 & 0 & 0 & 0 & 0 & C_{66} \end{bmatrix}$$
(3a)

where $C_{66} = \frac{1}{2} (C_{11} - C_{12})$,

$$\mathbf{e}^{t} = \begin{bmatrix} 0 & 0 & 0 & 0 & e_{24} & 0 \\ e_{31} & e_{31} & e_{33} & 0 & 0 & 0 \end{bmatrix}, \text{ and } \boldsymbol{\varepsilon}^{S} = \begin{bmatrix} \varepsilon_{11} & 0 \\ 0 & \varepsilon_{33} \end{bmatrix}$$
 (3b)

The dynamic governing equations of the disk are derived using the generalized Hamilton's principle for electromechanical systems, written as [44,45].

$$\int_{0}^{t} \left(\delta T - \delta \Pi + \delta W_{\text{ele}} + \delta W \right) \, \mathrm{d}t = 0 \tag{4}$$

with the variation of kinetic energy δT , given by

$$\delta T = \iiint_{V} \delta \dot{\mathbf{U}}^{t} \rho \dot{\mathbf{U}} \, dV, \tag{5}$$

where $\mathbf{U} = \left\{ u \mid w \right\}^t$ is the displacement field. The variation of potential energy due to strain is given by $\delta \mathbf{\Pi} = \iiint_V \delta \mathbf{S}^t \boldsymbol{\sigma} dV$ and is rewritten using Eq. (1a) as

$$\delta \Pi = \iiint_{V} \left(\delta \mathbf{S}^{t} \mathbf{C}^{E} \mathbf{S} - \delta \mathbf{S}^{t} \mathbf{e} \mathbf{E} \right) \, \mathrm{d}V, \tag{6}$$

The variation of electrical energies given by $\delta W_{\text{ele}} = \iiint_V \delta \mathbf{E}^t \mathbf{D} dV$ is rewritten using Eq. (1b) as

$$\delta W_{\text{ele}} = \iiint_{V} \left(\delta \mathbf{E}^{t} \mathbf{e}^{t} \mathbf{S} + \delta \mathbf{E}^{t} \varepsilon^{S} \mathbf{E} \right) \, \mathrm{d}V, \tag{7}$$

The variational work done by external forces including structural damping and pressure distribution due to the acoustic structure interaction with the surrounding fluid is written as

$$\delta W = -\iiint_{V} \delta \mathbf{U}^{t} c_{d} \dot{\mathbf{U}} \, dV - \sum_{l} Q_{p} \delta \varphi - \int_{0}^{D/2} 2\pi r \delta \mathbf{U}^{t} |_{z=t/2} \left\{ \begin{matrix} 0 \\ P_{T} \end{matrix} \right\} \, dr$$

$$+ \int_{0}^{D/2} 2\pi r \delta \mathbf{U}^{t} |_{z=-t/2} \left\{ \begin{matrix} 0 \\ P_{R} \end{matrix} \right\} \, dr - \int_{-t/2}^{t/2} \pi D \delta \mathbf{U}^{t} |_{r=D/2} \left\{ \begin{matrix} P_{C} \\ 0 \end{matrix} \right\} \, dz$$

$$(8)$$

where c_d and Q_p are respectively the damping parameter, and point charges at the electrodes; P_T , P_B , and P_C are respectively the pressure on the top surface, bottom surface, and cylindrical boundary of the disk. Substituting Eqs. (5)–(8) into Eq. (4), we obtain

$$\iiint_{V} \left(\delta \mathbf{U}^{t} \rho \ddot{\mathbf{U}} - \delta \mathbf{S}^{t} \mathbf{C}^{E} \mathbf{S} + \delta \mathbf{S}^{t} \mathbf{e} \mathbf{E} + \delta \mathbf{E}^{t} \mathbf{e}^{t} \mathbf{S} + \delta \mathbf{E}^{t} \epsilon^{S} \mathbf{E} - \delta \mathbf{U}^{T} c_{d} \dot{\mathbf{U}} \right) dV - \sum Q_{p} \delta \varphi
- \int_{0}^{D/2} 2\pi r \delta \mathbf{U}_{z=t/2}^{t|} \begin{Bmatrix} 0 \\ P_{T} \end{Bmatrix} dr + \int_{0}^{D/2} 2\pi r \delta \mathbf{U}_{z=-t/2}^{t|} \begin{Bmatrix} 0 \\ P_{B} \end{Bmatrix} dr
- \int_{-t/2}^{t/2} \pi D \delta \mathbf{U}_{r=D/2}^{t|} \begin{Bmatrix} P_{C} \\ 0 \end{Bmatrix} dz = 0$$
(9)

2.1. Finite element analysis

Numerical solution of the above problem is obtained by applying the Finite Element Method to the meridional plane of the disk which constitutes a rectangular domain of $0 \le r \le D/2$, and $-t/2 \le z \le t/2$. As suggested by Ragab and Fayed [46], each element is mapped to a canonical bi-quadratic element in $\xi \eta$ space. The displacement vector is rewritten as

$$\mathbf{U}(r,z,t) \equiv \mathbf{U}(\xi,\eta,t) = \boldsymbol{\psi}_{II}\mathbf{U}^{\varrho} \tag{10a}$$

and electric potential is rewritten as

$$\varphi(r, z, t) \equiv \varphi(\xi, \eta, t) = \psi_{\alpha} \varphi^{e} \tag{10b}$$

where the ψ_U , and ψ_{φ} are respectively the displacement, and electrical potential shape function matrices; \mathbf{U}^e , and φ^e are the nodal displacement, and electrical potential vectors of an element. Consequently, Eq. (2a), and (b) are rewritten as

$$S = BU^{e}, \qquad E = -B_{m}\varphi^{e} \tag{11}$$

The complete expressions for $\psi_{\mathbf{U}}$, ψ_{φ} , \mathbf{U}^{e} , φ^{e} , \mathbf{B} , and \mathbf{B}_{φ} are presented in Appendix A. Substituting Eq. (11) into the variational statement presented in Eq. (9), we obtain the elemental matrix governing (actuation) equation as

$$\mathbf{M}^{e}\ddot{\mathbf{U}}^{e} + \mathbf{K}_{\mathbf{u}\mathbf{u}}^{e} \mathbf{U}^{e} + \mathbf{D}^{e}\dot{\mathbf{U}}^{e} + \mathbf{K}_{\mathbf{u}\boldsymbol{\omega}}^{e}\boldsymbol{\varphi}^{e} + \mathbf{F}^{e} = 0$$
(12a)

and the corresponding sensing equation as

$$-\mathbf{K}_{\boldsymbol{\omega}\mathbf{u}}^{e}\mathbf{U}^{e}+\mathbf{K}_{\boldsymbol{\omega}\boldsymbol{\omega}}^{e}\boldsymbol{\varphi}^{e}=\mathbf{Q}^{e}$$
(12b)

where

$$\mathbf{M}^{e} = \iint 2\pi r \boldsymbol{\psi}_{\mathbf{U}}^{t} \rho \boldsymbol{\psi}_{\mathbf{U}} \, \mathrm{d}r \, \mathrm{d}z, \quad \mathbf{K}_{\mathbf{u}\mathbf{u}}^{e} = \iint 2\pi r \mathbf{B}^{t} \mathbf{C}^{E} \mathbf{B} \, \mathrm{d}r \, \mathrm{d}z, \tag{13a}$$

$$\mathbf{D}^{e} = \iint 2\pi r \boldsymbol{\psi}_{\mathbf{U}}^{t} c_{d} \boldsymbol{\psi}_{\mathbf{U}} \, \mathrm{d}r \, \mathrm{d}z, \quad \mathbf{K}_{\boldsymbol{\varphi}\boldsymbol{\varphi}}^{e} = \iint 2\pi r \mathbf{B}_{\boldsymbol{\varphi}}^{t} \boldsymbol{\varepsilon}^{S} \mathbf{B}_{\boldsymbol{\varphi}} \, \mathrm{d}r \, \mathrm{d}z, \tag{13b}$$

$$\mathbf{K}_{\mathbf{u}\boldsymbol{\varphi}}^{e} = \iint 2\pi r \mathbf{B}^{t} \mathbf{e} \mathbf{B}_{\boldsymbol{\varphi}} \, \mathrm{d}r \, \mathrm{d}z = \mathbf{K}_{\boldsymbol{\varphi}\mathbf{u}}^{e^{-t}}, \tag{13c}$$

$$\mathbf{F}^{e} = \int_{0}^{D/2} 2\pi r \boldsymbol{\psi}_{\mathbf{U}}^{t} \begin{Bmatrix} 0 \\ P_{T} \end{Bmatrix} dr - \int_{0}^{D/2} 2\pi r \boldsymbol{\psi}_{\mathbf{U}}^{t} \begin{Bmatrix} 0 \\ P_{B} \end{Bmatrix} dr + \int_{-t/2}^{t/2} \pi D \boldsymbol{\psi}_{\mathbf{U}}^{t} \begin{Bmatrix} P_{C} \\ 0 \end{Bmatrix} dz, \tag{13d}$$

and \mathbf{Q}^e is a vector of net charge at each point in the element. In deriving Eqs. (12a) and (12b), the natural boundary conditions are applied on the outer surfaces in the variational statement. In particular, the normal stresses are written as the surface acoustic pressure and zero shear stresses. It should be noted that the acoustic pressures, P_T , P_B , and P_C are unknown at the moment. By assembling all the elemental equations and imposing the symmetry conditions, u = 0 on the axis of the disk, we obtain the global governing equation as

$$\mathbf{M}\ddot{\mathbf{U}} + \alpha \mathbf{M}\dot{\mathbf{U}} + \mathbf{K}_{\mathbf{u}\mathbf{u}}\mathbf{U} + \mathbf{K}_{\mathbf{u}\boldsymbol{\varphi}}\boldsymbol{\varphi} + \mathbf{F} = 0 \tag{14a}$$

and the corresponding global sensing equation as

$$\mathbf{K}_{\alpha\mathbf{u}}\mathbf{U} + \mathbf{K}_{\alpha\alpha}\boldsymbol{\varphi} = \mathbf{Q} \tag{14b}$$

In writing Eq. (14a), a proportional damping $\mathbf{D} = \alpha \mathbf{M}$ is assumed.

The acoustic-structure interaction on the disk's surfaces due to the surrounding fluid is characterized by the resistive and reactive components of acoustic radiation impedance which are respectively manifested as radiation damping and radiation mass effects. These effects can be easily determined by comparing the electrical impedance measurement in air and in water. The electrical impedance in air is chosen as a reference because of its low relative acoustic impedance ($Z_{\rm air}/Z_{\rm disk}$) and that its acoustic loading effects on the response of the disk are insignificant. The evaluation of electrical impedance involves determining the electrical current passing through the disk for an input electric potential difference across the electrodes. We consider the top and bottom surfaces of the disk as electrodes and define the dynamic potential difference between them as φ_0 . Assuming the bottom electrode as the reference where the electrical potential is zero, the appropriate electrical boundary conditions are written as

$$\varphi = 0$$
, \forall bottom surface nodes, (15a)

$$\varphi = \varphi_0$$
, and $\sum_t Q = Q_0 \quad \forall \text{ top surface nodes},$ (15b)

where Q_0 is the net charge accumulated on the electrode and, by definition, is also the time integral of the current passing through the disk.

Inspecting Eqs. (14a), and (b), we note that they contain the electrical potential at all nodes, and that the electrical potential at the interior nodes is a dependent quantity on the displacement and excitation potential difference (φ_0). As such, we further simplify Eqs. (14a), and (b) by following the condensation technique [42,43] and obtain the final global governing equation as

$$\mathbf{M}\ddot{\mathbf{U}} + \alpha \mathbf{M}\dot{\mathbf{U}} + \hat{\mathbf{K}}_{\mathbf{H}\mathbf{u}}\mathbf{U} + \hat{\mathbf{K}}_{\mathbf{H}\mathbf{u}}\varphi_0 + \mathbf{F} = 0 \tag{16a}$$

and the corresponding sensing equation as

$$\hat{\mathbf{K}}_{\boldsymbol{\omega}\mathbf{u}}\mathbf{U} + \hat{\mathbf{K}}_{\boldsymbol{\omega}\boldsymbol{\omega}}\boldsymbol{\varphi}_0 = \mathbf{Q}_0 \tag{16b}$$

The vital steps followed in the condensation procedure and expressions for the coefficient matrices are detailed in Appendix B.

2.2. Acoustic loading

The electrical impedance can be computed from Eqs. (16a), and (b) once the acoustic loading vector **F** is determined. From Eq. (13d), one needs to obtain the pressure pattern generated on the surfaces of the disk to determine **F**. This involves a significant effort of solving the mass, and momentum equations of fluid dynamics in conjunction with the equation of state for the closed-form expression of pressure for a given displacement mode of the disk. Also, there is no closed-form expression to find pressure distribution on a freely suspended disk (i.e., unbaffled) of arbitrary dimensions. To address this challenge, we hypothesize that the pressure pattern of a particular mode in the fluid, referred to as modal pressure pattern, at the corresponding resonant frequency can be used to investigate the response characteristics near that frequency. As such, we employed COMSOL Multiphysics to obtain the pressure pattern in the frequency domain by assuming that the fluid is inviscid. This approach fails away from the resonant frequency of the considered mode for two main reasons. Firstly, the pressure pattern is a function of frequency (wavelength), and that it changes with the change in frequency. Secondly, a neighboring mode that possesses a different displacement field and corresponding modal pressure pattern than the mode considered can interfere with the modal pressure pattern considered to produce erroneous results. Our approach is justified because the disk is most efficient at the resonant frequency response and the computational cost can be significantly reduced when using only information at the resonant frequency to investigate the response near that modal frequency.

To model the effects of radiation damping and mass, we assume small amplitude acoustic waves and consequently, that the pressure variations on the surface and ultimately ${\bf F}$ can be represented in terms of the local normal velocity and acceleration. Also, when solved in the frequency domain, the real part of the velocity is maximum at the resonant frequency (damped resonant frequency, strictly speaking) and is approximately equal to the absolute value of the velocity. Unlike the velocity, the pressure manifests itself in a more complicated way with equally crucial real and imaginary parts for representing the acoustic-structure interaction. Noting these concepts, for a given complex displacement field u and w, and corresponding complex pressure distributions P_T , P_B , and P_C at the resonant frequency in fluid for a particular mode, say f_r , under electrical excitation, we obtain ${\bf F}$ and rewrite Eqs. (16a), and (b). First, we represent the surface pressure and displacement fields in the form of transfer functions as $P_T/\text{Re}(\dot{w})|_{f_r}$ for the top surface, $P_B/\text{Re}(\dot{w})|_{f_r}$ for the bottom surface, and $P_C/\text{Re}(\dot{u})|_{f_r}$ for the cylindrical boundary of the disk. Next, using the transfer functions, we rewrite Eq. (13d) as

$$\mathbf{F}^{e} = \int_{0}^{D/2} 2\pi r \operatorname{diag}\left(\boldsymbol{\psi}_{\mathbf{U}}^{t} \begin{Bmatrix} 0 \\ P_{T}/\operatorname{Re}(\dot{w})|_{f_{r}} \end{Bmatrix}\right) \dot{\mathbf{U}}^{e} \, \mathrm{d}r - \int_{0}^{D/2} 2\pi r \operatorname{diag}\left(\boldsymbol{\psi}_{\mathbf{U}}^{t} \begin{Bmatrix} 0 \\ P_{B}/\operatorname{Re}(\dot{w})|_{f_{r}} \end{Bmatrix}\right) \dot{\mathbf{U}} \, \mathrm{d}r + \int_{-t/2}^{t/2} \pi D \operatorname{diag}\left(\boldsymbol{\psi}_{\mathbf{U}}^{t} \begin{Bmatrix} P_{C}/\operatorname{Re}(\dot{u})|_{f_{r}} \end{Bmatrix}\right) \dot{\mathbf{U}}^{e} \, \mathrm{d}z$$

$$(17)$$

where **diag**({.}), and Re respectively represent the diagonal matrix of vector {.}, and real part of a complex number operator. Substituting the appropriate transfer functions acquired from COMSOL Multiphysics into Eq. (17), we obtain

$$\mathbf{F}^e = \mathbf{R}^e \dot{\mathbf{U}}^e + \mathbf{j} \mathbf{X}^e \dot{\mathbf{U}}^e \tag{18a}$$

where $i = \sqrt{-1}$. For a harmonic excitation with excitation frequency ω , the above equation is rewritten as

$$\mathbf{F}^e = \mathbf{R}^e \dot{\mathbf{U}}^e + \frac{1}{c} \mathbf{X}^e \ddot{\mathbf{U}}^e \tag{18b}$$

where \mathbf{R}^e , and \mathbf{X}^e are the elemental diagonal matrices obtained, respectively, from the real and imaginary parts of the right hand side of Eq. (17). Substituting Eq. (18b) into elemental governing Eq. (14a), assembling all the elemental equations and imposing the symmetry conditions, we obtain the final global governing equation as

$$\left(\mathbf{M} + \frac{1}{\alpha}\mathbf{X}\right)\ddot{\mathbf{U}} + (\alpha\mathbf{M} + \mathbf{R})\dot{\mathbf{U}} + \hat{\mathbf{K}}_{\mathbf{u}\mathbf{u}}\mathbf{U} + \hat{\mathbf{K}}_{\mathbf{u}\boldsymbol{\varphi}}\boldsymbol{\varphi}_0 = 0 \tag{19a}$$

and the corresponding global sensing equation as

$$\widehat{\mathbf{K}}_{\boldsymbol{\varphi}\mathbf{U}}\mathbf{U} + \widehat{K}_{\boldsymbol{\varphi}\boldsymbol{\varphi}}\boldsymbol{\varphi}_0 = Q_0 \tag{19b}$$

For a harmonic electrical actuation of $\varphi_0 = \overline{\varphi}_0 e^{j\omega t}$, substituting the corresponding response, $\mathbf{U} = \overline{\mathbf{U}} e^{j\omega t}$, and accumulated charge, $Q_0 = \overline{I}_0 e^{j\omega t}/(j\omega)$ into Eqs. (19a), and (19b) the electrical impedance is derived as

$$\frac{\varphi_0}{I_0} = \frac{1}{j\omega \left[-\hat{\mathbf{K}}_{\boldsymbol{\varphi}\mathbf{u}} \left(\hat{\mathbf{K}}_{\mathbf{u}\mathbf{u}} - \omega^2 \left(\mathbf{M} + \frac{1}{\omega} \mathbf{X} \right) + j\omega \left(\alpha \mathbf{M} + \mathbf{R} \right) \right]^{-1} \hat{\mathbf{K}}_{\mathbf{u}\boldsymbol{\varphi}} + \hat{K}_{\boldsymbol{\varphi}\boldsymbol{\varphi}} \right]}$$
(20)

where $I_0 (= dQ_0/dt)$ is the amplitude of the current passing through the piezoelectric disk.

2.3. Reduced-order model: mode projection

Reduced-order modeling of a continuous vibration system involves determining the of exact solution to the unforced, undamped, and short-circuited integro-partial differential equations followed by a Galerkin weighted residual method to obtain an ordinary differential equation of the temporal modal coordinate. The variational statement in Eq. (9) provides the integro-partial differential governing and sensing equations of the disk. However, in its raw form without imposing any assumptions on the dimensions of the disk [26–30] it doesn't possess a closed-form solution, impacting the ability to derive a reduced-order model. To solve this challenge, we use the matrix equation (19a) and study the free vibration problem $\mathbf{M}\ddot{\mathbf{U}} + \hat{\mathbf{K}}_{\mathbf{u}\mathbf{u}}\mathbf{U} = 0$ to obtain the axisymmetric eigenvalues and eigenvectors. The eigenvectors are then used to determine the governing equation of the temporal modes. Further, if the modes are widely spaced, then the displacement vector near the resonant frequency of a particular mode is approximated by

$$\mathbf{U} \approx q(t)\mathbf{V}(r,z) \tag{21}$$

where q(t), and **V** are respectively the temporal coordinate and mass-normalized eigenvector of the considered mode. Multiplying the governing equation by \mathbf{V}^t and using Eq. (21), we obtain the governing equation of the temporal modal coordinate as

$$\ddot{q}\left(1 + \frac{X_{\text{mode}}}{\omega}\right) + \left(2\zeta\omega_n + R_{\text{mode}}\right)\dot{q} + \omega_n^2 q + \hat{\theta}\varphi_0 = 0 \tag{22a}$$

$$-\widehat{\theta}q + C_p^S \varphi_0 = Q_0 \tag{22b}$$

where

$$X_{\text{mode}} = \mathbf{V}^t \mathbf{X} \mathbf{V}, \quad R_{\text{mode}} = \mathbf{V}^t \mathbf{R} \mathbf{V},$$
 (22c)

$$\widehat{\theta} = \mathbf{V}^t \widehat{\mathbf{K}}_{\mathbf{u}\boldsymbol{\varphi}} = -\widehat{\mathbf{K}}_{\boldsymbol{\varphi}\mathbf{u}} \mathbf{V}, \quad 2\zeta \omega_n = \alpha, \quad \text{and} \quad C_p^S = \widehat{K}_{\boldsymbol{\varphi}\boldsymbol{\varphi}}$$
 (22d)

Here, C_p^S is the equivalent capacitance of the piezoelectric disk at constant strain, which cannot be measured by simply connecting the wires of a freely hanging disk in air to a capacitance meter. This ambiguity is due to the negligible relative acoustic impedance of air and piezoelectric disk (i.e., $Z_{\rm air}/Z_{\rm disk}$ << 1) that makes the surfaces of the disk effectively traction-free. Consequently, the capacitance meter measures the capacitance at a constant stress, $C_p^\sigma (\neq C_p^S)$. Using Eqs. (22a), and (22b), we derive the electrical impedance as

$$\frac{\varphi_0}{I_0} = \left[C_p^S j\omega + \frac{j\widehat{\theta}^2 \omega}{-\omega^2 \left(1 + X_{\text{mode}}/\omega \right) + j \left(2\zeta \omega_n + R_{\text{mode}} \right) \omega + \omega_n^2} \right]^{-1}$$
(23)

It is relevant to point out that the electrical impedance derived from the FEM model in Eq. (20), and the one obtained from ROM mentioned in Eq. (23) can only predict the impedance and, therefore, the response in the fluid with reasonable accuracy near the resonant frequency of the mode whose transfer functions are acquired from COMSOL Multiphysics. Although FEM has the capability to predict the impedance for all the vibrational modes of the disk for the case when fluid damping is non-existent, we note that in deriving Eq. (20), the acoustic-structure interaction was limited to a particular mode, thereby limiting the FEM model's capability to model the response at all modes in fluids. Finally, the advantage of the ROM over the FEM is that the determination of the effect of fluid on the response characteristics of the disk requires estimates of only two parameters, namely $X_{\rm mode}$, and $R_{\rm mode}$, instead of diagonal matrices or transfer functions as would be required in the FEM model. In the following sections, different case studies are presented to validate the FEM method and evaluate the effectiveness of the derived reduced-order model.

3. Experimental setup, results and validation of the reduced-order model

The acoustic radiation effects on the piezoelectric disk by surrounding fluid are investigated by comparing the disk's electrical impedance in air and water.

3.1. Experiments in air

In the first set of experiments, the versatility and accuracy of the FEM model in predicting the response characteristics of the disk were investigated using both qualitative and quantitative analysis. In the qualitative analysis, the vibrational mode shapes obtained from experiments in air are compared to those predicted by the FEM model. Whereas in the quantitative analysis, the electrical impedance in air as determined from the FEM model is validated with the experimentally measured values. The predicted response for specific electrical actuation is then compared to the measured response. We considered two different piezoelectric ceramic disks APC760, and APC472 made of Navy type - II (PZT - 5A) material manufactured by APC International, Ltd for the in-air experiments. The two disks differed primarily in their dimensions. Their material and geometric properties

Table 1 The list of geometric and material properties of the disks considered. ε^{τ} is the permittivity of vacuum.

Parameter	APC472	APC760	APC196	APC1116
D [mm]	11.4	9.5	19	9.9
t [mm]	10.6	3.9	2.3	1
ρ [kg/m ³]	7700	7700	7700	7700
C_{11} [GPa]	154.13	172.14	174.05	175.22
C_{12} [GPa]	105	105	110	110
C_{13} [GPa]	93.7	110.1	99.9	99.9
C_{33} [GPa]	115.82	135.6	123	123
C_{44} [GPa]	23	23	30.1	30.1
$e_{31} [C/m^2]$	-3.86	-3.24	-3.05	-2.8
$e_{33} [C/m^2]$	19.3	19.04	15.14	14.7
$e_{24} [C/m^2]$	11.64	11.64	9.86	9.86
ϵ_{11}/ϵ_r	1130	1243	910.8	993.6
ϵ_{33}/ϵ_r	914	1005.4	770	840
α [1/s]	9937.41	18070.99	2581.94	6600

are presented in Table 1. The disks were suspended freely with wires, as shown in Fig. 1b. The vibrational mode shapes were measured using a Polytec PSV -500 Scanning Vibrometer while the voltage excitation and data acquisition were performed using the PSV-500 front end interface. The sampling frequency and frequency resolution were respectively set to 5.12 MHz 156.25 Hz. The response to an electrical excitation provided by Keysight 33500B signal generator was measured using Polytech OFV 5000/505 laser Doppler vibrometer (LDV) in conjunction with NI DAQ system (PCI -6115 and BNC -2110). The LDV data was sampled at 4 MHz.

Fig. 2a, c, e, g and i present the top surface's mode shape of the first five modes of APC760 disk at two instants with a phase difference of π as measured by the scanning laser when excited using a periodic chirp voltage signal. The free vibration of Eq. (16a) (i.e., $\mathbf{M}\ddot{\mathbf{U}} + \hat{\mathbf{K}}_{mu}\mathbf{U} = 0$) is solved by defining a 10 \times 8 mesh, and using the material properties of APC760 disk that are presented in Table 1 to obtain the mode shapes predicted by the FEM model. The $m \times n$ mesh refers to m and n bi-quadratic elements respectively in the radial and thickness directions. The mesh size is chosen as a compromise between convergence in eigenvalues (natural frequencies) and computational cost. Moreover, both symmetric and anti-symmetric modes (see Aggarwal [26,27] for details) were predicted by the FEM. However, only the symmetric nodes participate in the electromechanical coupling and can be excited with electrical excitation. As such, we consider the top surface's mode shape of the first five symmetrical modes predicted by the FEM model presented in Fig. 2b, d, f, h, and j and show the excellent qualitative agreement with their FEM counterparts that are presented respectively in Fig. 2a, c, e, g, and i. From Fig. 2h, we note that the mean displacement of the top surface of fourth symmetrical mode is non-zero and hence we identify it as a thickness extensional mode [31,32]. Further, by noting the diameter to thickness ratio of the APC760 disk, D/t = 2.44, the results in Fig. 2g and h reaffirm that the mode shape of the thickness mode of a disk can be drastically different from a "piston-like" profile. Although none of the mode shapes resemble a "piston-like" behavior, we note that the first mode which is often referred to as length expander (LE) mode [33] shown in Fig. 2a and b is closest to "piston-like" deformation. Furthermore, because the LE mode doesn't posses any nodal rings or anti-nodes like the higher modes, and that the resonant frequencies are in the ultrasonic range, it is reasonable to assume that this mode will possess highest radiation efficiency. As such, although the proposed approach can be applied to any mode of interest, we will focus on the LE mode in the subsequent sections.

The electrical impedance measurements are preformed for parameter identification and to assess the acoustic loading effects. Electrical impedance is chosen because it entails the information of all key material parameters that impact the vibrational response such as, the natural frequency, electromechanical coupling term, and capacitance. Moreover, by matching the electrical impedance, the corresponding surface velocity response can be accurately predicted. To this end, we validate the fidelity of the proposed approach and model through comparison with the measured electrical impedance of the APC472 and APC760 disks. The electrical impedance of the freely-hanging APC472 disk in air was measured using HP4192A impedance analyzer over the frequency range of 0–300 kHz. By defining a 6 \times 10 mesh, the measured impedance was matched with FEM model's prediction using Eq. (20) (with X = R = 0, as the medium is air) with emphasis on the length expander mode and adjusted material properties that are presented in Table 1. From Fig. 3a, we note a discrepancy in the amplitude of the electrical impedance near the open-circuit frequency of the LE mode as well as the second symmetrical mode. This discrepancy is attributed to the different damping ratios of the short- and open-circuit conditions of LE mode and second mode. Using Eq. (19a), the velocity of the center of the disk's top surface normalized to excitation voltage amplitude is evaluated near the short-circuit resonant frequency of the LE mode ranging over the frequency range of 110-115 kHz. As shown in Fig. 3b, the results from the FEM model are in agreement with the measurements made using the scanning laser. A similar procedure was performed on an APC760 disk. A very close agreement of the electrical impedance and velocity of the center of the disk's top surface obtained by the FEM model and determined experimentally are presented, respectively, in Fig. 3c and d. The plots show excellent agreement of the predicted impedance to the measured one. Based on the plots in Fig. 3a-d, we have experimentally validated that by satisfying the electrical impedance using the FEM model, the response characteristics are automatically satisfied. We exploit this notion and investigate only the electrical impedance in the forthcoming case studies.

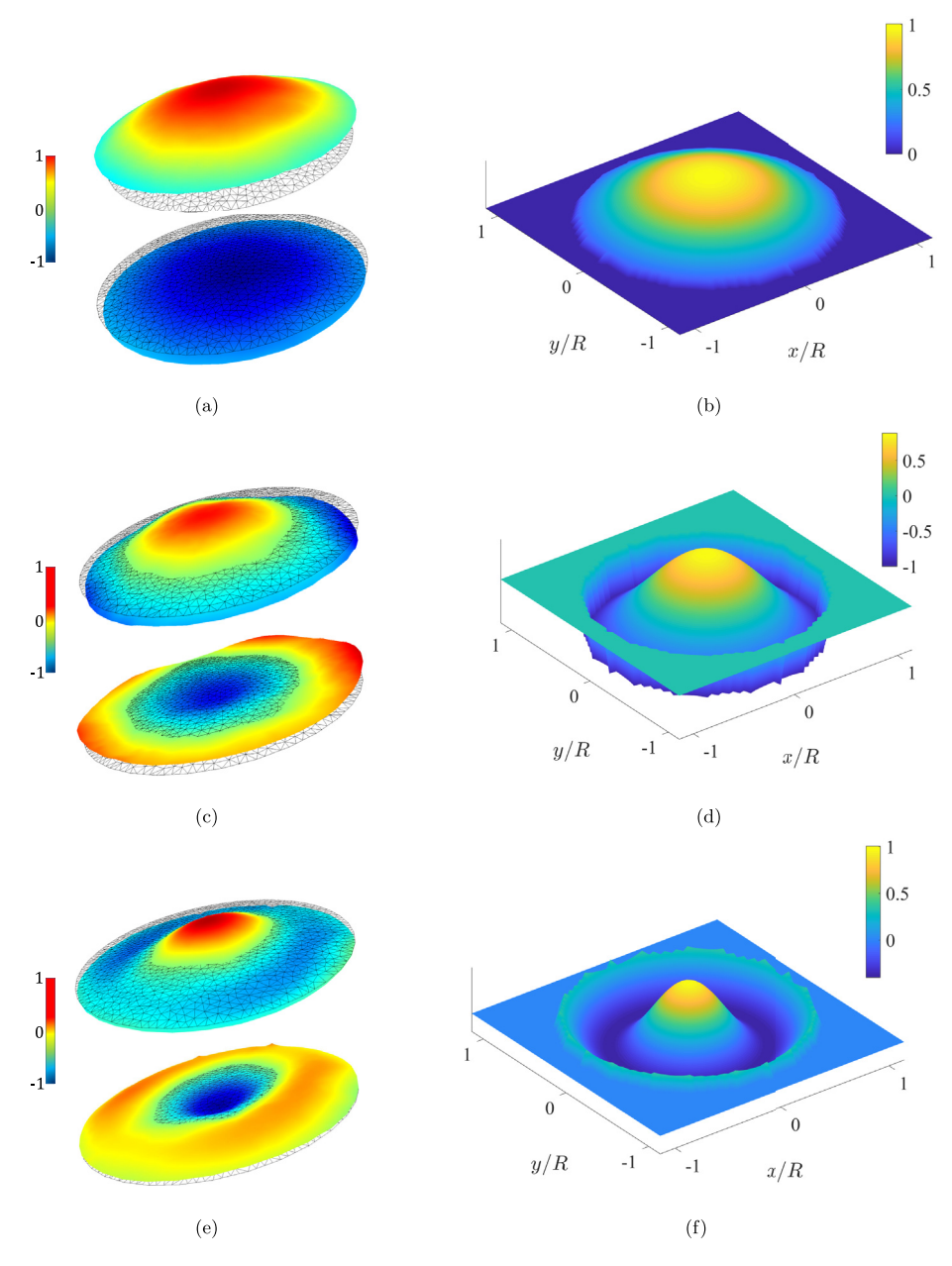


Fig. 2. The top surface's displacement mode shapes of APC760 disk for the first three symmetrical modes obtained from (a,c,e) experiments at 193.4 kHz, 333.1 kHz, and 400.8 kHz respectively, and by (b,d,f) FEM model. The top surface's displacement mode shapes of APC760 disk for the fourth, and fifth symmetrical modes obtained from (g,i) experiments at 494.4 kHz and 601.1 kHz respectively, and by (h,j) FEM model.

3.2. Experiments in water

For in-water validation, we consider four different piezoelectric ceramic disks namely APC472, APC760, APC196, and APC1116, which differ in dimensions, namely the D/t ratio, to investigate the acoustic loading characteristics by water on the LE mode. The geometric and material properties of the disks are mentioned in Table 1. The electrical impedance measurements were made using HP4192A impedance analyzer by submerging the disks under deionized water, to avoid electrical shorting, in a tank of dimensions 615 mm \times 318 mm \times 325 mm. The inner surfaces of the tank were partially covered with Aptflex F28 acoustic absorbing sheets manufactured by Precision Acoustics Ltd. to minimize surface acoustic reflections from the walls.

Recalling that the approach and reduced-order model presented here are based on the finite element method, which requires transfer functions, we investigated the disk's response under water using COMSOL Multiphysics to solve the acoustic structure interaction problem by imposing pressure and velocity continuity boundary conditions at the interface. We constructed 2–D

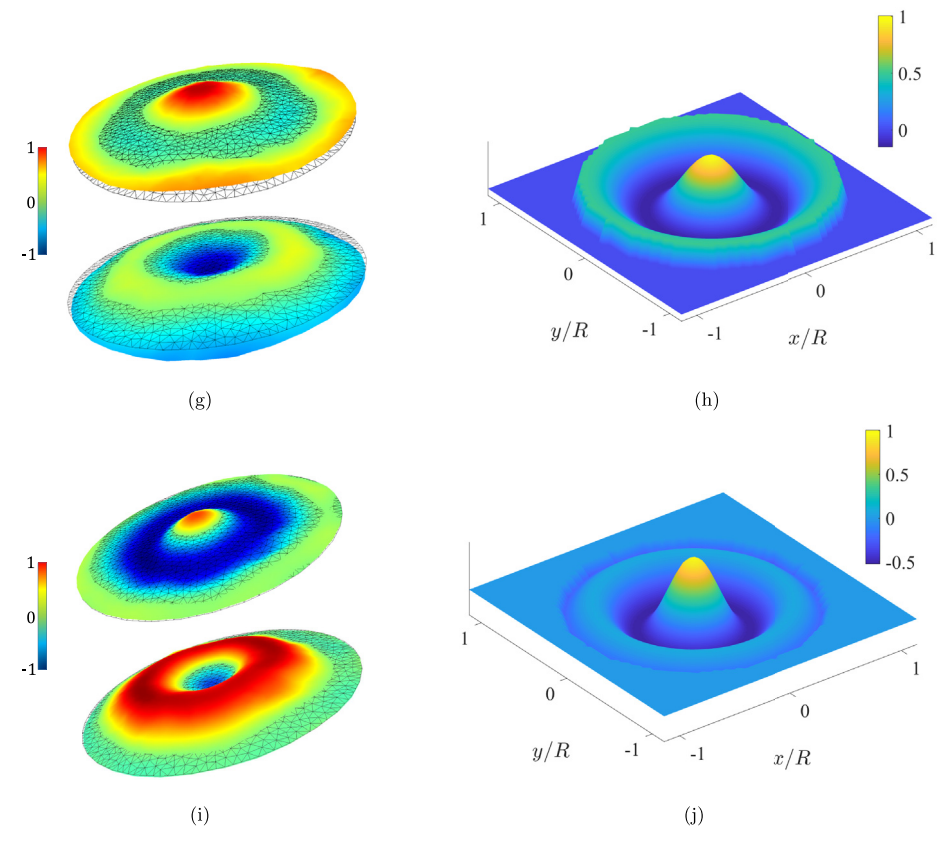


Fig. 2. Continued

axisymmetric cases where the radius is six times the maximum wavelength, λ_{\max} . Moreover, to simulate infinite medium conditions, we included a perfectly matched layer of thickness equal to λ_{\max} . Also, the maximum size of the triangular mesh element was chosen such that there are at least ten nodes in the minimum wavelength. The material properties were determined by matching the electrical impedance in the air. It is relevant to point out that, in general, finding the exact set of parameters that govern the behavior of the piezoelectric disk requires sophisticated optimization schemes. However, the disks were excited electrically and their functioning frequency can be considered as the short-circuit resonant frequency. As such, we matched the electrical impedance near the short-circuit frequency. For the open-circuit conditions, we limited the matching only to the resonant frequency. Following the methodology proposed in Section 2.2, we recorded the complex pressure on the surfaces of the disk, and the real part of the surface velocities at the resonant frequency of the LE mode in water and determined the transfer functions. As an example, the pressure and velocity distributions for APC472 disk when actuated with an excitation voltage of 1 V under water are shown in Fig. 4. In particular, Fig. 4a and d shows the real and imaginary parts of the pressure for the top and the cylindrical boundary of the disk, respectively, and Fig. 4b and e shows respectively the corresponding real part of surface velocities at 108.35 kHz, which is the resonant frequency of LE mode in water. The obtained transfer functions $P_T/\text{Re}(\dot{w})$, and $P_C/\text{Re}(\dot{u})$ are respectively presented in Fig. 4c and f. It should be noted that for symmetrical modes, $P_B/\text{Re}(\dot{w})$ for the bottom surface is equal to $-P_T/\text{Re}(\dot{w})$ for the top surface. We used the transfer functions to construct the **R** and **X** matrices as described in Eq. (17) - (19a). Finally, the R_{mode} and X_{mode} were determined by using **R**, and **X** matrices as outlined in Section 2.3. The procedure mentioned above was repeated for five different diameters using the material properties of each disk and fixing the D/t ratio. The results of R_{mode}/ω_n and X_{mode}/ω_n are respectively summarized in Fig. 5a and b that show a decrease in the radiation damping and radiation mass when increasing the D/t ratio. Fig. 5a and b also show a trend in the normalized radiation damping and radiation mass effects with a near-zero slope for a given D/t ratio. The results suggest that the radiation mass and damping effects in water are independent of the diameter of the disk for a given aspect ratio. The efficacy of proposed ROM is shown next by presenting the results for APC472 and APC760 disks.

Fig. 6a shows the electrical impedance measured in air and underwater for APC472 disk. A significant variation in the amplitude and a slight leftward shift in the resonant frequencies are noted. By inspecting Eqs. (20), and (23) we relate the variation in amplitude to radiation damping (i.e., \mathbf{R} , and R_{mode}), and leftward shift in resonant frequencies to the radiation mass (i.e., \mathbf{X} , and X_{mode}). The FEM model's and the ROM's predictions of the electrical impedance in the air using the identified material parameters are presented in Fig. 6b along with the experimental measurement, which shows agreement near the short-circuit resonant frequency of the LE mode. However, the ROM doesn't accurately predict the response at the open-circuit resonant

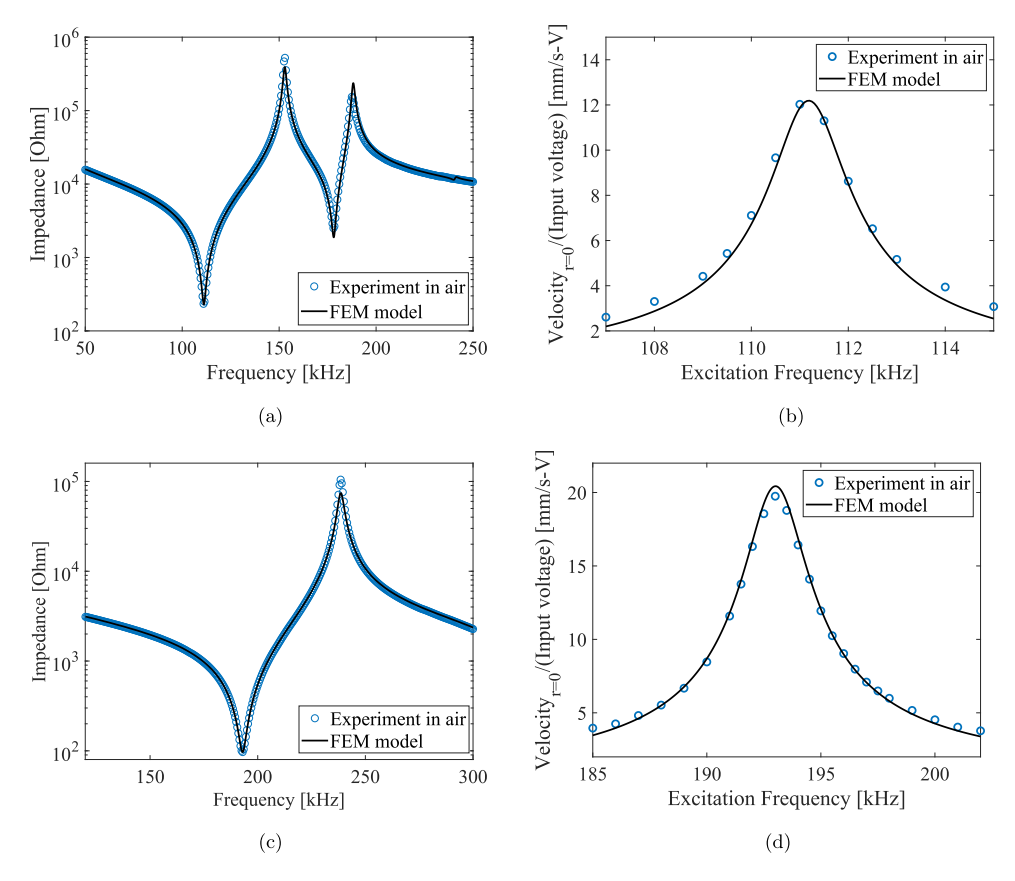


Fig. 3. Comparison between the experimental data and FEM model's predictions of the absolute value of electrical impedance and frequency response function (FRF) of normalized velocity of the disk's center for (a,b) APC472 and (c,d) APC760 disks. The normalization is done using the excitation voltage amplitude, and R = D/2.

frequency of the LE mode and completely misses the second symmetric mode exhibited by APC472 disk highlighting the important anticipated shortcomings of the ROM. The two main reasons for the shortcomings are (a) the ROM was provided only with the eigenvalues of the LE mode corresponding to short-circuit frequency, and moreover (b) the mode shape is not conserved between short and open-circuit resonant frequencies for a given mode [33], which results in improper estimation of modal electromechanical coupling, $\hat{\theta}$. But, nevertheless, the ROM is able to accurately predict the behavior at the short-circuit resonant frequency, which in turn, is the application frequency for electrical actuation, which is the focus of the current investigation. Fig. 6c shows excellent agreement between the measured electrical impedance and that predicted from COMSOL Multiphysics, FEM model, and ROM for a considerably broad range near the short-circuit resonant frequencies. This is a remarkable result as the ROM is a single DOF system using only two parameters to obtain the same result by COMSOL Multiphysics which is computationally costly by several orders. We also note from Fig. 6c that there is a reasonable discrepancy in the predictions made by COMSOL Multiphysics at the open-circuit resonant frequencies. The reasons for this discrepancy are multifold. It could have been manifested due to non-uniqueness of the adjustments made to the material parameters, to the shortcoming of proportional damping as discussed earlier, or due to neglecting the viscous effects.

The results of the investigation performed on APC760 disk are presented in Fig. 7a - c. The plots in these figures were obtained using the same approach used for Fig. 6a, b, and c. Once again, the emphasis was on the short-circuit range while correcting the material properties provided by the manufacturer through matching with the FEM model's predictions of the electrical impedance in air to that obtained from experiments. Due to the absence of any nearby mode in APC760 disk, the agreement of prediction of the electrical impedance in DI water by COMSOL Multiphyics solver, FEM model, and ultimately ROM to that obtained from experiments is much better than that of APC472 disk which is shown in Fig. 7c. We found that the results of investigating APC196 and APC1116 disks presented respectively in Figs. 8a-8c and 9a-9c are very similar to the results of the APC472, and APC196 disks. They are presented in Appendix C.

The emphasis in this work has been on electrical actuation of the piezoelectric disk, which best represents the transmitter in UAET systems. We note that the electrical impedance doesn't include the effects of reflection and diffraction of the incident acoustic field which manifest in the case of a receiver. Moreover, in a general piezoelectric system, the resonant frequency corresponding to the global optimum load resistance occurs between short and open-circuit resonant frequencies [47]. The approach presented in this paper utilizes the eigenvalues (or modeshapes), and pressure distributions at short-circuit resonant

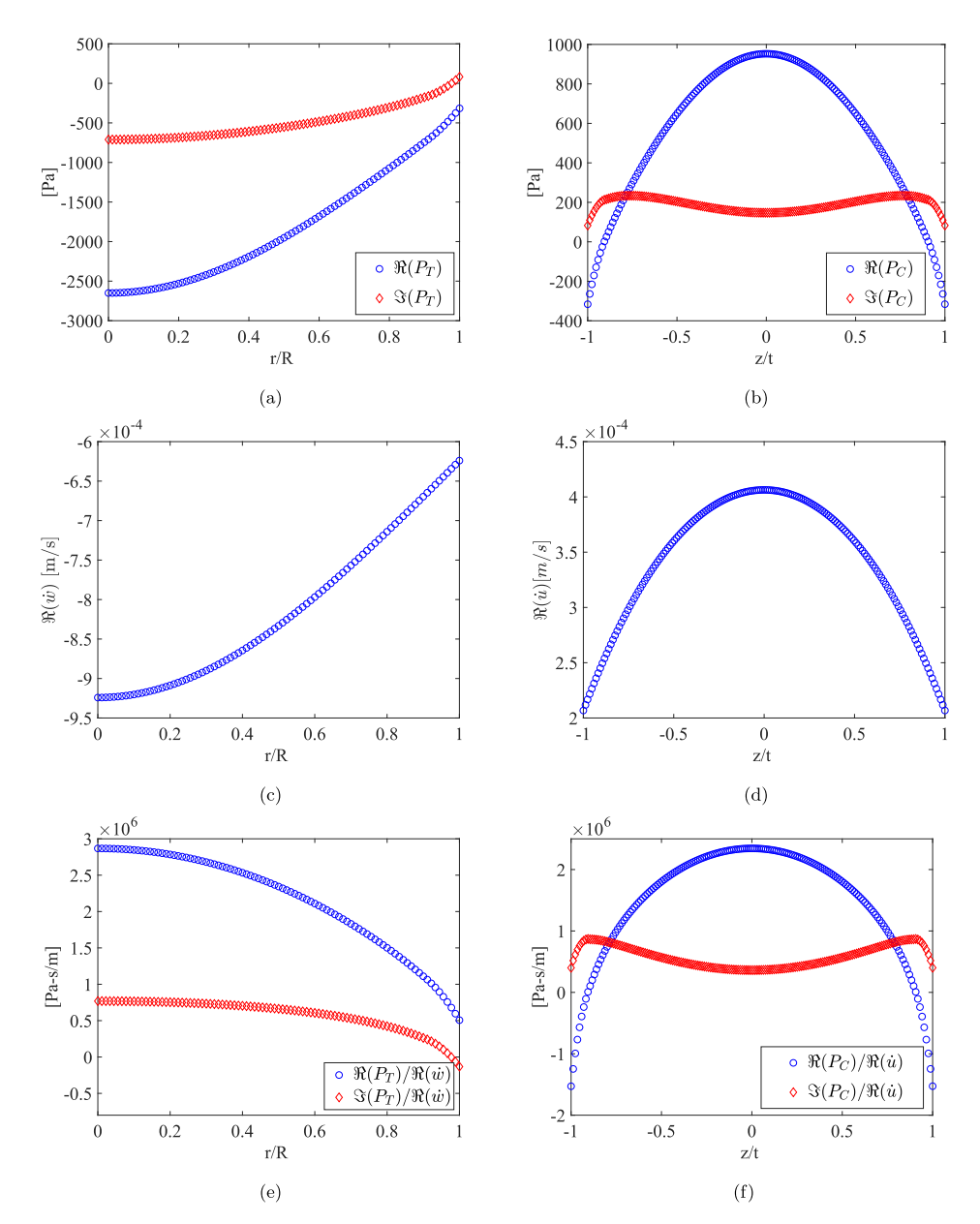


Fig. 4. The pressure distribution, real part of normal velocity, and their transfer function, respectively, of (a,c,e) top and (b,d,f) cylindrical surfaces.

frequency. To analyze the performance of a receiver one needs to account for different physics and make the following changes. The first change is that the acoustic loading vector **F**, should be determined using the surface pressure distributions associated with a given source at the resonant frequency corresponding to the optimum load resistance. Also, **F** is now the sum of excitation force due to the incident acoustic field, blocked pressure (reflection and diffraction), and acoustic loading effects due to self radiation pressure of the receiver. If one assumes an acoustic source facing the top surface of the receiver, then the self radiation pressure can be differentiated from incident pressure field, reflections, and scattering by inspecting the pressure fields on the top and bottom surfaces. This assumption is justified because, in an infinite medium, there would be no reflections on the bottom surface of the receiver. Now, if the ROM obtained using eigenvalues at short-circuit resonant frequency is not accurate, one can use the eigenvalues at the open-circuit resonant frequency. The eigenvalues for open-circuit conditions in the air are determined by recasting Eqs. (19a), and (b) as [42].

$$\mathbf{M}\ddot{\mathbf{U}} + \left(\widehat{\mathbf{K}}_{\mathbf{u}\mathbf{u}} - \widehat{\mathbf{K}}_{\mathbf{u}\boldsymbol{\varphi}}\widehat{\mathbf{K}}_{\boldsymbol{\varphi}\mathbf{u}}/\widehat{K}_{\boldsymbol{\varphi}\boldsymbol{\varphi}}\right)\mathbf{U} = \mathbf{0}$$
 (24)

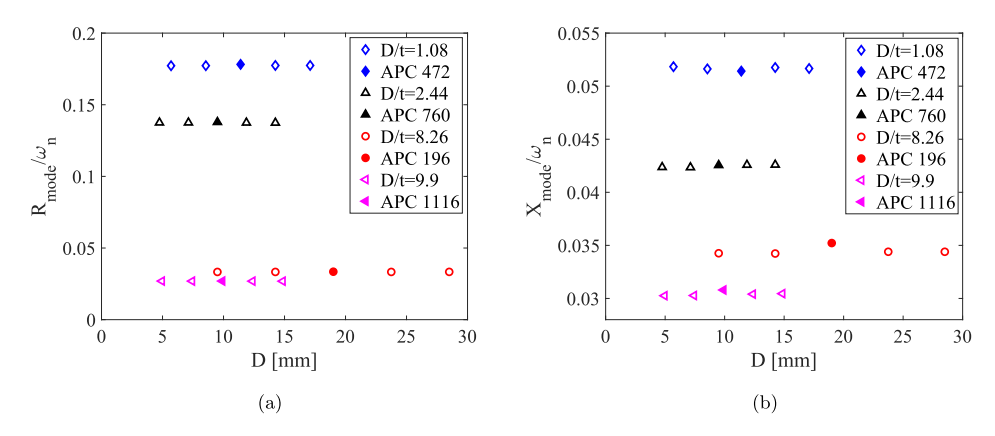


Fig. 5. (a) Radiation damping, and (b) Radiation mass variations as a function of diameter of the disk in water normalized to corresponding angular short-circuit frequency for the length expander mode in air obtained from numerical simulations in COMSOL Multiphysics solver. Four different diameters are chosen by fixing the D/t ratio and materials properties of the disks mentioned in table I. The solid and hollow markers respectively represent the disk mentioned in Table 1 and other diameters considered for analysis.

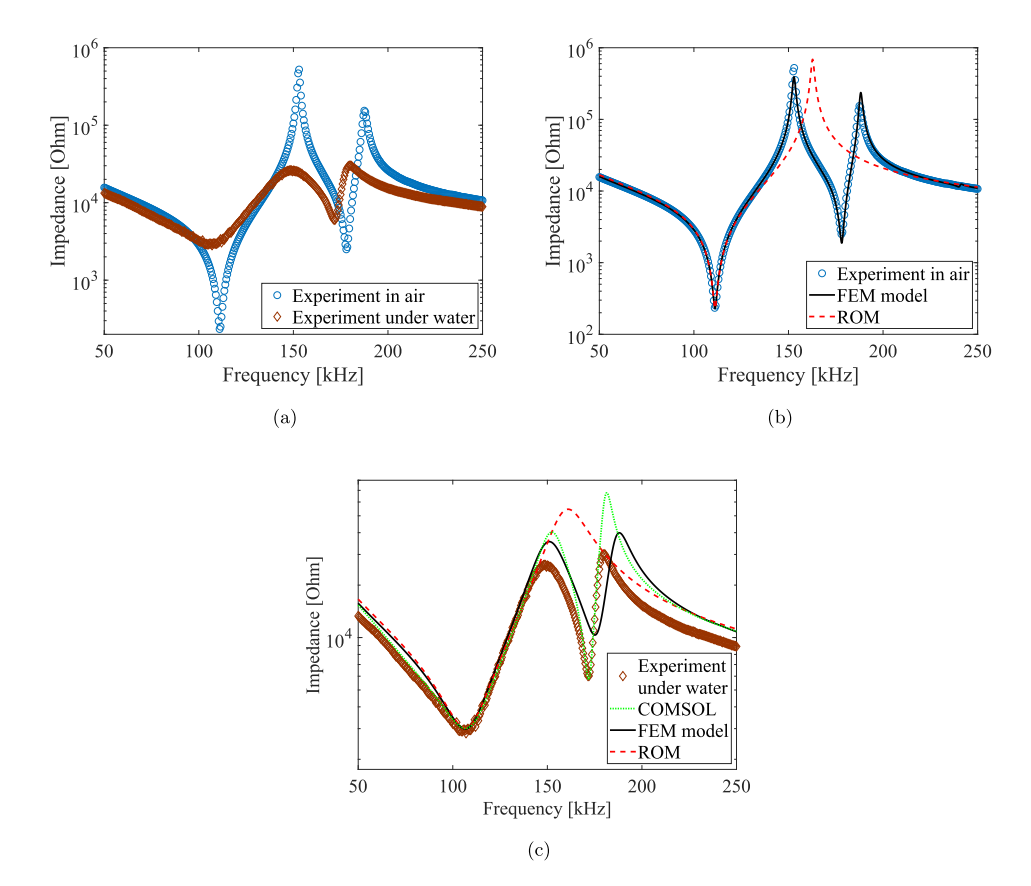


Fig. 6. Comparison of electrical impedance (a) measured in air with that obtained under water, (b) measured in air with that predicted by the FEM model, and ROM, (c) measured under water with that predicted by COMSOL Multiphysics solver, FEM model, and ROM for APC472 disk.

4. Conclusions

A mathematical framework was presented to evaluate the response of resonant vibration modes of piezoelectric disks in UAET systems. Particular attention was paid for developing a reduced-order model (ROM) that can capture the acoustic loading effects on the piezoelectric disk submerged in a fluid domain under electrical actuation. In order to accurately model the underlying physics, we presented a formulation that determines the ROM from a finite element model (FEM). The acoustic loading

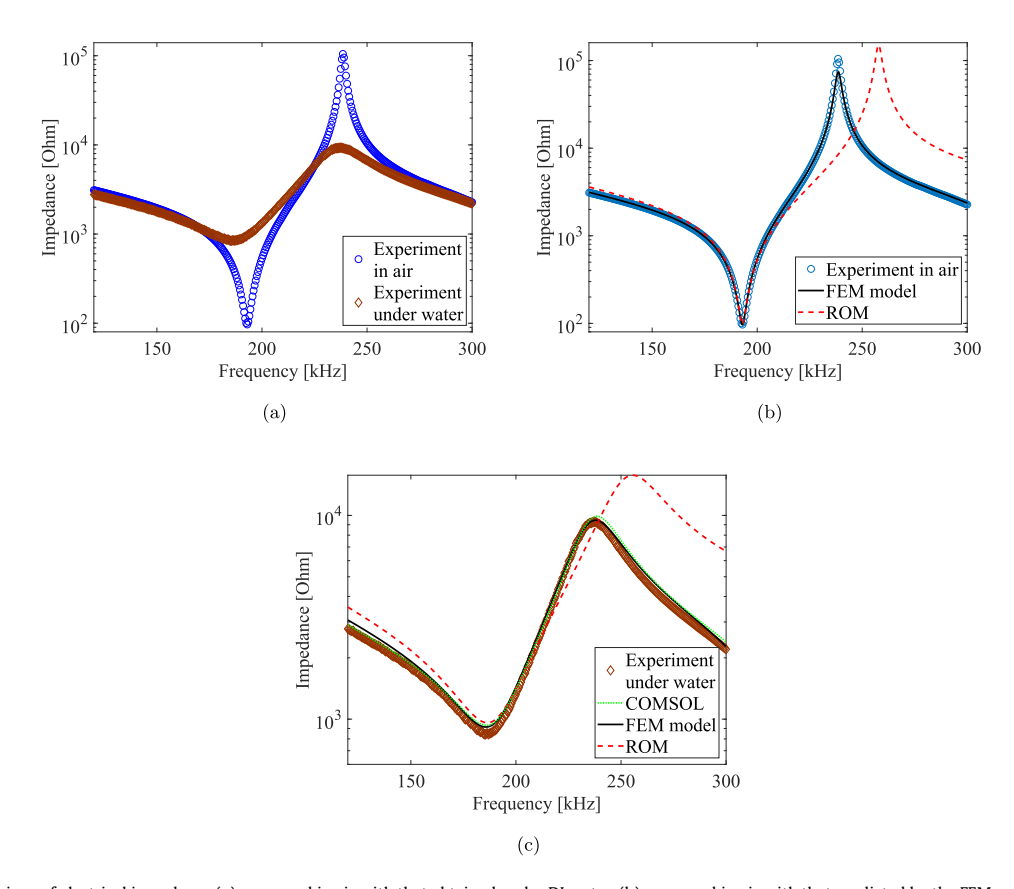


Fig. 7. Comparison of electrical impedance (a) measured in air with that obtained under DI water, (b) measured in air with that predicted by the FEM model, and ROM, (c) measured under DI water with that predicted by COMSOL Multiphysics solver, FEM model, and ROM for APC760 disk.

effects were modeled in the ROM as the two parameters, namely $R_{\rm mode}$ and $X_{\rm mode}$ that respectively quantify radiation damping, and mass radiation effects. With the knowledge of $R_{\rm mode}$ and $X_{\rm mode}$, the need for computationally expensive numerical solvers is eliminated. Parameter identification was done by matching the electrical impedance measurements in air with the FEM's predictions, which satisfied the vibration response of the disk, as well. We then examined the efficacy of the proposed ROM by comparing the electrical impedance of four piezoelectric disks that have different aspect ratios as predicted by the ROM to that obtained from experiments near the short-circuit resonant frequency. We found that the normalized radiation mass, and damping effects for a given diameter to thickness ratio, and material properties of the transmitter disk have a very weak dependence on the variation of the diameter. However, the acoustic structure interaction effects are different for the receiver disk, which is excited by an incident acoustic field generated by a transmitter. The proposed ROM in this paper can be modified for the receiver disk in the case of acoustic excitation. This work paves the way to develop ROMs that provide closed-form expressions for the vibration responses and electrical power output, which are crucial for the design and performance optimization of UAET systems. This research improves the understanding of the fundamental aspects of the UAET process. The results can be successfully applied towards the development of new and disruptive UAET technologies with a significant impact on the overall energy efficiency of UAET systems.

5. Compliance with ethical standards - conflict of interest

The authors declare that they have no conflict of interest.

CRediT authorship contribution statement

Vamsi C. Meesala: Conceptualization, Methodology, Software, Validation, Formal analysis, Investigation, Data curation, Writing - original draft, Visualization. **Saad Ragab:** Writing - review & editing, Methodology. **Muhammad R. Hajj:** Conceptualization, Writing - review & editing, Supervision, Funding acquisition. **Shima Shahab:** Conceptualization, Writing - review & editing, Supervision, Funding acquisition, Project administration.

Acknowledgements

This work was supported by the National Science Foundation Grant No. ECCS –1711139, which is gratefully acknowledged. The authors express their gratitude to Dr. Prashant Kumar for his cordial assistance with the scanning laser vibrometer.

Appendices A. Matrices

$$\psi_{\mathbf{U}} = \begin{bmatrix} \psi_1 & 0 & 0 & \dots & \psi_9 & 0 & 0 \\ 0 & \psi_1 & 0 & \dots & 0 & \psi_9 & 0 \end{bmatrix}$$
 (25)

$$\mathbf{U}^e = \left\{ u_1 w_1 \dots u_9 w_9 \right\}^t \tag{26}$$

$$\boldsymbol{\psi}_{\boldsymbol{\varphi}} = \left\{ \psi_1 \dots \psi_9 \right\} \tag{27}$$

$$\boldsymbol{\varphi}^e = \left\{ \varphi_1 \dots \varphi_9 \right\}^t \tag{28}$$

$$\mathbf{B} = \begin{bmatrix} \frac{\partial \psi_1}{\partial r} & 0 & \dots & \frac{\partial \psi_9}{\partial r} & 0\\ \frac{\psi_1}{r} & 0 & \dots & \frac{\psi_9}{r} & 0\\ 0 & \frac{\partial \psi_1}{\partial z} & \dots & 0 & \frac{\partial \psi_9}{\partial z}\\ 0 & 0 & \dots & 0 & 0\\ \frac{\partial \psi_1}{\partial z} & \frac{\partial \psi_1}{\partial r} & \dots & \frac{\partial \psi_9}{\partial z} & \frac{\partial \psi_9}{\partial r}\\ 0 & 0 & \dots & 0 & 0 \end{bmatrix}$$

$$(29)$$

$$\mathbf{B}_{\varphi} = \begin{cases} \frac{\partial \psi_1}{\partial r} & \dots & \frac{\partial \psi_9}{\partial r} \\ \frac{\partial \psi_1}{\partial z} & \dots & \frac{\partial \psi_9}{\partial z} \end{cases}$$
(30)

Appendices B. Condensation

The condensation procedure employed to simplify governing Eq. (14a), and corresponding sensing Eq. (14b), respectively, to Eqs. (16a), and (b) is presented in this Appendix. From the boundary conditions mentioned in Eq. (15a), the potential on bottom surface is zero, and hence the corresponding row in $\mathbf{K}_{\mathbf{u}\boldsymbol{\varphi}}$ and $\mathbf{K}_{\boldsymbol{\varphi}\boldsymbol{\varphi}}$ are deleted in further analysis. We then relate the unknown potential of internal nodes to their corresponding displacements. To this end, Eq. (14a) is rewritten as

$$\mathbf{M}\ddot{\mathbf{U}} + \mathbf{K}_{\mathbf{u}\mathbf{u}}\mathbf{U} + \alpha\mathbf{M}\dot{\mathbf{U}} + \mathbf{K}_{\mathbf{u}\boldsymbol{\varphi}\mathbf{i}}\boldsymbol{\varphi}_{\mathbf{i}} + \mathbf{K}_{\mathbf{u}\boldsymbol{\varphi}\mathbf{t}}\boldsymbol{\varphi}_{\mathbf{t}} + \mathbf{F} = 0$$
(31a)

and Eq. (14b) is rewritten as

$$-\mathbf{K}_{i\boldsymbol{\omega}\mathbf{u}}\mathbf{U} + \mathbf{K}_{\boldsymbol{\omega}\boldsymbol{\omega}\mathbf{i}i}\boldsymbol{\varphi}_{\mathbf{i}} + \mathbf{K}_{\boldsymbol{\omega}\boldsymbol{\omega}\mathbf{i}i}\boldsymbol{\varphi}_{\mathbf{t}} = 0 \tag{31b}$$

$$-\mathbf{K}_{t\omega\mathbf{u}}\mathbf{U} + \mathbf{K}_{\omega\omega\mathbf{t}i}\boldsymbol{\varphi}_{\mathbf{i}} + \mathbf{K}_{\omega\omega\mathbf{t}t}\boldsymbol{\varphi}_{\mathbf{t}} = \mathbf{Q}_{\mathbf{t}} \tag{31c}$$

where the subscripts i, and t, respectively, stand for interior, and top nodes. From Eq. (31b), the potential of internal nodes is rewritten as

$$\varphi_{\mathbf{i}} = -\mathbf{K}_{\varphi\varphi\mathbf{i}\mathbf{t}}^{-1} \left(\mathbf{K}_{\varphi\varphi\mathbf{i}\mathbf{t}} \varphi_{\mathbf{t}} - \mathbf{K}_{\mathbf{i}\varphi\mathbf{u}} \mathbf{U} \right) \tag{32}$$

By adding all the rows in Eq. (31c) and from the electrical boundary conditions mentioned in Eq. (15b), we obtain

$$-\sum_{\text{row}} \mathbf{K}_{\mathbf{t}\boldsymbol{\varphi}\mathbf{u}} \mathbf{U} + \sum_{\text{row}} \mathbf{K}_{\boldsymbol{\varphi}\boldsymbol{\varphi}\mathbf{t}\mathbf{i}} \boldsymbol{\varphi}_{\mathbf{i}} + \sum_{\text{row}} \mathbf{K}_{\boldsymbol{\varphi}\boldsymbol{\varphi}\mathbf{t}\mathbf{t}} \mathbf{I} \boldsymbol{\varphi}_{0} = Q_{0}$$
(33)

where I is a unit column vector. Eq. (33) is further simplified using Eq. (32) to obtain the sensing Eq. (16b) as

$$\widehat{\mathbf{K}}_{\boldsymbol{\varphi}\mathbf{u}}\mathbf{U} + \widehat{\mathbf{K}}_{\boldsymbol{\varphi}\boldsymbol{\varphi}}\boldsymbol{\varphi}_0 = Q_0 \tag{34}$$

where

$$\widehat{\mathbf{K}}_{\boldsymbol{\varphi}\mathbf{u}} = -\sum_{row} \mathbf{K}_{\boldsymbol{t}\boldsymbol{\varphi}\mathbf{u}} + \left(\sum_{row} \mathbf{K}_{\boldsymbol{\varphi}\boldsymbol{\varphi}\mathbf{t}\mathbf{i}}\right) \mathbf{K}_{\boldsymbol{\varphi}\boldsymbol{\varphi}\mathbf{i}\mathbf{i}}^{-1} \mathbf{K}_{\mathbf{i}\boldsymbol{\varphi}\mathbf{u}},$$

and

$$\widehat{\mathbf{K}}_{\boldsymbol{\varphi}\boldsymbol{\varphi}} = (\sum_{row} \mathbf{K}_{\boldsymbol{\varphi}\boldsymbol{\varphi}\mathbf{t}\mathbf{t}} - \left(\sum_{row} \mathbf{K}_{\boldsymbol{\varphi}\boldsymbol{\varphi}\mathbf{t}\mathbf{i}}\right) [\mathbf{K}_{\boldsymbol{\varphi}\boldsymbol{\varphi}\mathbf{i}\mathbf{i}}^{-1} \mathbf{K}_{\boldsymbol{\varphi}\boldsymbol{\varphi}\mathbf{i}\mathbf{t}}])\mathbf{I}$$

By using Eq. (32), Eq. (31a) is rewritten to obtain the governing Eq. (16a) as

$$\mathbf{M}\ddot{\mathbf{U}} + \alpha \mathbf{M}\dot{\mathbf{U}} + \hat{\mathbf{K}}_{\mathbf{u}\mathbf{u}}\mathbf{U} + \hat{\mathbf{K}}_{\mathbf{u}\boldsymbol{\varphi}}\varphi_0 + \mathbf{F} = 0 \tag{35}$$

where

$$\widehat{\mathbf{K}}_{\mathbf{u}\mathbf{u}} = \mathbf{K}_{\mathbf{u}\mathbf{u}} + \mathbf{K}_{\mathbf{u}\boldsymbol{\varphi}\mathbf{i}}\mathbf{K}_{\boldsymbol{\varphi}\boldsymbol{\varphi}\mathbf{i}\mathbf{i}}^{-1}\mathbf{K}_{\mathbf{i}\boldsymbol{\varphi}\mathbf{u}},$$

and

$$\widehat{\mathbf{K}}_{\mathbf{u}\boldsymbol{\varphi}} = \left(\mathbf{K}_{\mathbf{u}\boldsymbol{\varphi}\mathbf{t}} - \mathbf{K}_{\mathbf{u}\boldsymbol{\varphi}\mathbf{i}}\mathbf{K}_{\boldsymbol{\varphi}\boldsymbol{\varphi}\mathbf{i}\mathbf{i}}^{-1}\mathbf{K}_{\boldsymbol{\varphi}\boldsymbol{\varphi}\mathbf{i}\mathbf{t}}\right)\mathbf{I}$$

Appendices C. More results

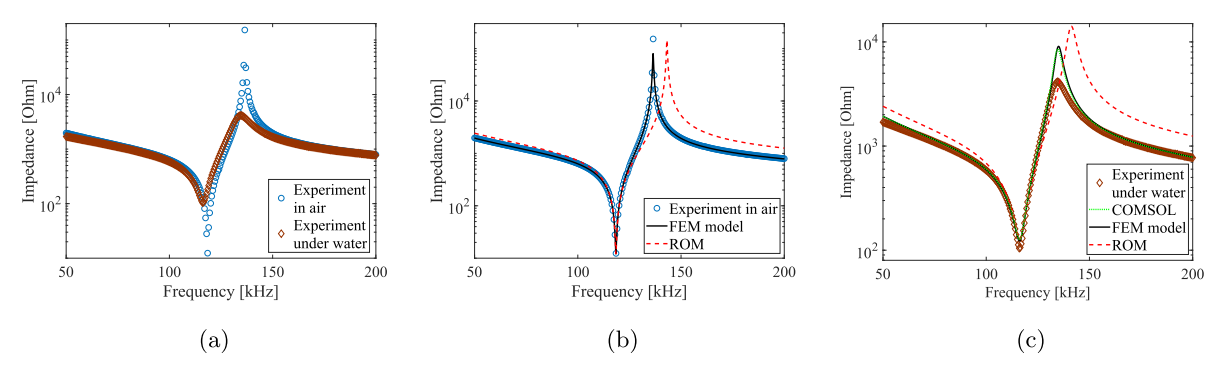


Fig. 8 Comparison of electrical impedance (a) measured in air with that obtained under DI water, (b) measured in air with that predicted by the FEM model, and ROM, (c) measured under DI water with that predicted by COMSOL Multiphysics solver, FEM model, and ROM for APC196 disk.

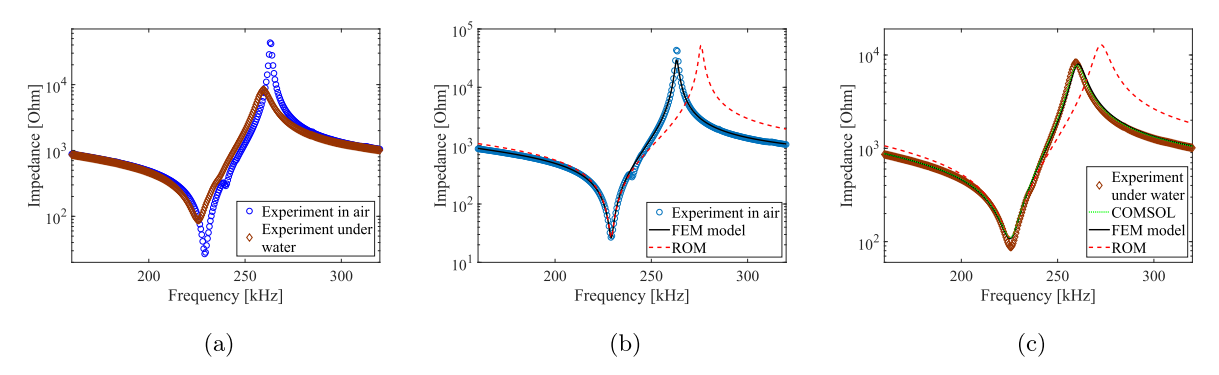


Fig. 9 Comparison of electrical impedance (a) measured in air with that obtained under DI water, (b) measured in air with that predicted by the FEM model, and ROM, (c) measured under DI water with that predicted by COMSOL Multiphysics solver, FEM model, and ROM for APC1116 disk.

Declaration of interests

The authors declare that they have no known competing financial interests or personal relationships that could have appeared to influence the work reported in this paper.

References

- [1] M.G. Roes, J.L. Duarte, M.A. Hendrix, E.A. Lomonova, Acoustic energy transfer: a review, IEEE Trans. Ind. Electron. 60 (1) (2013) 242–248.
- [2] J.L. Villa, J. Salln, A. Llombart, J.F. Sanz, Design of a high frequency inductively coupled power transfer system for electric vehicle battery charge, Appl. Energy 86 (3) (2009) 355–363.
- [3] Z. Bi, T. Kan, C.C. Mi, Y. Zhang, Z. Zhao, G.A. Keoleian, A review of wireless power transfer for electric vehicles: prospects to enhance sustainable mobility, Appl. Energy 179 (2016) 413–425.
- [4] J. Deng, B. Pang, W. Shi, Z. Wang, A new integration method with minimized extra coupling effects using inductor and capacitor series-parallel compensation for wireless ev charger, Appl. Energy 207 (2017) 405–416.
- [5] P. Maharjan, M. Salauddin, H. Cho, J.Y. Park, An indoor power line based magnetic field energy harvester for self-powered wireless sensors in smart home applications, Appl. Energy 232 (2018) 398–408.
- [6] M. Jafari, Z. Malekjamshidi, J. Zhu, Design and development of a multi-winding high-frequency magnetic link for grid integration of residential renewable energy systems, Appl. Energy 242 (2019) 1209–1225.
- [7] X. Yu, S. Sandhu, S. Beiker, R. Sassoon, S. Fan, Wireless energy transfer with the presence of metallic planes, Appl. Phys. Lett. 99 (21) (2011) 214102.
- [8] S. Kim, J.S. Ho, L.Y. Chen, A.S. Poon, Wireless power transfer to a cardiac implant, Appl. Phys. Lett. 101 (7) (2012) 073701.
- [9] A. Kurs, A. Karalis, R. Moffatt, J.D. Joannopoulos, P. Fisher, M. Soljai, Wireless power transfer via strongly coupled magnetic resonances, Science 317 (5834) (2007) 83–86.
- [10] P. Valdastri, E. Susilo, T. Forster, C. Strohhofer, A. Menciassi, P. Dario, Wireless implantable electronic platform for chronic fluorescent-based biosensors, IEEE Trans. Biomed. Eng. 58 (6) (2011) 1846–1854.
- [11] Y. Vaiarello, W. Tatinian, Y. Leduc, N. Veau, G. Jacquemod, Ultra-low-power radio microphone for cochlear implant application, IEEE J. Emerg. Select. Top. Circuit. Syst. 1 (4) (2011) 622–630.
- [12] T. Maleki, N. Cao, S.H. Song, C. Kao, S.-C. Ko, B. Ziaie, An ultrasonically powered implantable micro-oxygen generator (imog), IEEE Trans. Biomed. Eng. 58 (11) (2011) 3104–3111.
- [13] K.L. Lee, C.-P. Lau, H.-F. Tse, D.S. Echt, D. Heaven, W. Smith, M. Hood, First human demonstration of cardiac stimulation with transcutaneous ultrasound energy delivery: implications for wireless pacing with implantable devices, J. Am. Coll. Cardiol. 50 (9) (2007) 877–883.
- [14] D. Seo, J.M. Carmena, J.M. Rabaey, M.M. Maharbiz, E. Alon, Model validation of untethered, ultrasonic neural dust motes for cortical recording, J. Neurosci. Methods 244 (2015) 114–122.
- [15] J. Charthad, M.J. Weber, T.C. Chang, A. Arbabian, A mm-sized implantable medical device (imd) with ultrasonic power transfer and a hybrid bi-directional data link, IEEE J. Solid State Circ. 50 (8) (2015) 1741–1753.
- [16] J. Charthad, T.C. Chang, Z. Liu, A. Sawaby, M.J. Weber, S. Baker, F. Gore, S.A. Felt, A. Arbabian, A mm-sized wireless implantable device for electrical stimulation of peripheral nerves, IEEE Trans. Biomed. Circuit. Syst. 12 (2) (2018) 257–270.
- [17] L. Jiang, Y. Yang, R. Chen, G. Lu, R. Li, J. Xing, K.K. Shung, M.S. Humayun, J. Zhu, Y. Chen, et al., Ultrasound-induced wireless energy harvesting for potential retinal electrical stimulation application, Adv. Funct. Mater. (2019) 1902522.
- [18] S. Baltsavias, W. Van Treuren, M. J. Weber, J. Charthad, S. Baker, J. L. Sonnenburg, A. Arbabian, In Vivo Wireless Sensors for Gut Microbiome Redox Monitoring, arXiv preprint arXiv:1902.07386.
- [19] S. Ozeri, D. Shmilovitz, S. Singer, C.-C. Wang, Ultrasonic transcutaneous energy transfer using a continuous wave 650 khz Gaussian shaded transmitter, Ultrasonics 50 (7) (2010) 666–674.
- [20] S. Shahab, A. Erturk, Contactless ultrasonic energy transfer for wireless systems: acoustic-piezoelectric structure interaction modeling and performance enhancement, Smart Mater. Struct. 23 (12) (2014) 125032.
- [21] S. Shahab, M. Gray, A. Erturk, Ultrasonic power transfer from a spherical acoustic wave source to a free-free piezoelectric receiver: modeling and experiment, J. Appl. Phys. 117 (10) (2015) 104903.
- [22] M. Gorostiaga, M. Wapler, U. Wallrabe, Analytic model for ultrasound energy receivers and their optimal electric loads, Smart Mater. Struct. 26 (8) (2017) 085003
- [23] M. Gorostiaga, M. Wapler, U. Wallrabe, Analytic model for ultrasound energy receivers and their optimal electric loads ii: experimental validation, Smart Mater. Struct. 26 (10) (2017) 105021.
- [24] M. Bakhtiari-Nejad, A. Elnahhas, M.R. Hajj, S. Shahab, Acoustic holograms in contactless ultrasonic power transfer systems: modeling and experiment, J. Appl. Phys. 124 (24) (2018) 244901.
- [25] V.C. Meesala, M.R. Hajj, S. Shahab, Modeling and identification of electro-elastic nonlinearities in ultrasonic power transfer systems, Nonlinear Dynam. (2019) 1–20.
- [26] R.R. Aggarwal, Axially symmetric vibrations of a finite isotropic disk. i, J. Acoust. Soc. Am. 24 (5) (1952) 463-467.
- [27] R.R. Aggarwal, Axially symmetric vibrations of a finite isotropic disk. ii, J. Acoust. Soc. Am. 24 (6) (1952) 663-666.
- [28] P. Schnabel, Dispersion of thickness vibrations of piezoceramic disk resonators, IEEE Trans. Son. Ultrason. 25 (1) (1978) 16–23.
- [29] C.-H. Huang, Y.-C. Lin, C.C. Ma, Theoretical analysis and experimental measurement for resonant vibration of piezoceramic circular plates, IEEE Trans. Ultrason. Ferroelectrics Freq. Contr. 51 (1) (2004) 12–24.
- [30] A. Allam, K. Sabra, A. Erturk, Comparison of various models for piezoelectric receivers in wireless acoustic power transfer, in: Active and Passive Smart Structures and Integrated Systems XII, vol. 10967. International Society for Optics and Photonics, 2019, p. 109670S.
- [31] N. Guo, The Vibration Characteristics of Piezoelectric Discs, Ph.D. thesis, University of London, 1989.
- [32] N. Guo, P. Cawley, D. Hitchings, The finite element analysis of the vibration characteristics of piezoelectric discs, J. Sound Vib. 159 (1) (1992) 115–138.
- [33] H. Kunkel, S. Locke, B. Pikeroen, Finite-element analysis of vibrational modes in piezoelectric ceramic disks, IEEE Trans. Ultrason. Ferroelectrics Freq. Contr. 37 (4) (1990) 316–328.
- [34] N.D. Perreira, D. Dawe, An analytical model for noise generated by axial oscillations of unbaffled cylindrical elements, J. Acoust. Soc. Am. 75 (1) (1984) 80–87.
- [35] M.C. Junger, D. Feit, Sound, Structures, and Their Interaction, vol. 225, MIT press Cambridge, MA, 1986.
- [36] S. Suzuki, S. Maruyama, H. Ido, Boundary element analysis of cavity noise problems with complicated boundary conditions, J. Sound Vib. 130 (1) (1989) 79–96.
- [37] K. Fyfe, F. Ismail, An investigation of the acoustic properties of vibrating finite cylinders, J. Sound Vib. 128 (3) (1989) 361–375.
- [38] C. Audoly, Some aspects of acoustic interactions in sonar transducer arrays, J. Acoust. Soc. Am. 89 (3) (1991) 1428–1433.
- [39] H. Lee, R. Singh, Acoustic radiation from out-of-plane modes of an annular disk using thin and thick plate theories, J. Sound Vib. 282 (12) (2005) 313–339.
- [40] M. Caresta, Structural and Acoustic Responses of a Submerged Vessel, Lap Lambert Academic Publ, 2012.
- [41] Y.-H. Kim, Sound Propagation: an Impedance Based Approach, John Wiley & Sons, 2010.
- [42] H. Allik, K.M. Webman, J.T. Hunt, Vibrational response of sonar transducers using piezoelectric finite elements, J. Acoust. Soc. Am. 56 (6) (1974) 1782–1791.
- [43] D. Boucher, M. Lagier, C. Maerfeld, Computation of the vibrational modes for piezoelectric array transducers using a mixed finite element-perturbation method, IEEE Trans. Son. Ultrason. 28 (5) (1981) 318–329.
- [44] S.H. Crandall, Dynamics of Mechanical and Electromechanical Systems, McGraw-Hill, 1968.
- [45] N.W. Hagood, W.H. Chung, A. Von Flotow, Modelling of piezoelectric actuator dynamics for active structural control, J. Intell. Mater. Syst. Struct. 1 (3) (1990) 327–354.
- [46] S.A. Ragab, H.E. Fayed, Introduction to Finite Element Analysis for Engineers, CRC Press, 2017.
- [47] A. Erturk, D.J. Inman, Piezoelectric Energy Harvesting, John Wiley & Sons, 2011.